Nano Energy 73 (2020) 104836

Contents lists available at ScienceDirect

Nano Energy

journal homepage: http://www.elsevier.com/locate/nanoen

Li_2CO_3 effects: New insights into polymer/garnet electrolytes for dendrite-free solid lithium batteries

Hanyu Huo [a,b,d], Xiaona Li [a], Yipeng Sun [a], Xiaoting Lin [a], Kieran Doyle-Davis [a], Jianwen Liang [a], Xuejie Gao [a], Ruying Li [a], Huan Huang [d], Xiangxin Guo [c,**], Xueliang Sun [a,*]

[a] Department of Mechanical and Materials Engineering, University of Western Ontario, Ontario, N6A 5B9, Canada
[b] State Key Laboratory of High Performance Ceramics and Superfine Microstructure, Shanghai Institute of Ceramics, Chinese Academy of Sciences, Shanghai, 200050, China
[c] College of Physics, Qingdao University, Qingdao, 266071, China
[d] Glabat Solid-State Battery Inc., 700 Collip Circle, London, ON, N6G 4X8, Canada

ARTICLE INFO

Keywords:
Garnet electrolytes
Li_2CO_3
Li^+ transport pathways
Dendrite suppression
Solid-state batteries

ABSTRACT

Garnet particles are usually introduced into polymer matrices as fillers to fabricate polymer/garnet composite electrolytes (PGEs), which can not only improve the ionic conductivity but also enhance the mechanical strength to suppress Li dendrites. However, the surface Li_2CO_3 contamination of garnet particles through air exposure has long been overlooked when fabricating the PGEs. Considering the ultralow ionic conductivity and low oxidation voltage of Li_2CO_3, the effects of Li_2CO_3 should be taken into consideration. Herein, the PGEs with Li_2CO_3-containing and Li_2CO_3-free garnet particles are fabricated from "garnet-in-polymer" (GIP) to "polymer-in-garnet" (PIG) electrolyte compositions. The results indicate that Li^+ can be transported faster along the polymer/garnet interface in the Li_2CO_3-free GIP electrolytes, while Li^+ migration through the garnet bulk can be improved in the Li_2CO_3-free PIG electrolytes. The Lewis acid-base interactions between garnet and polymer are enhanced due to the Li_2CO_3 removal, thus increasing the Li^+ transference number. Furthermore, cathode-supported solid-state batteries with vertically aligned $LiFePO_4$ cathodes and Li_2CO_3-free PIG electrolytes are constructed, which show excellent rate and cycle performance. This work provides new insights into PGEs and the effects of Li_2CO_3, which can guide the improved design of PGEs for dendrite-free solid garnet batteries.

1. Introduction

The Nobel prize in chemistry 2019 was awarded jointly to three scientists for the development of lithium-ion batteries (LiBs) [1]. Thanks to the wide application of LiBs in portable electronics and electric vehicles, LiBs have become the ubiquitous choice for energy storage technology [2,3]. With current limitations, higher energy density and improved safety are required. Solid-state batteries (SSBs) consisting of Li metal anodes, solid-state electrolytes (SSEs) and high-voltage cathodes are one of the most promising candidates, which can provide higher energy density than traditional liquid-based LiBs [4]. Furthermore, the use of SSEs to substitute the flammable organic electrolytes can further enhance the safety of working batteries.

As one of the key components, various SSEs have been researched for decades, such as sulfide-type, NASICON-type, and garnet-type materials [5–7]. Among them, garnet SSEs have received much attention because of their excellent ionic conductivities at ambient temperature and high chemical/electrochemical stability against Li metal anodes [8,9]. Solid garnet electrolytes generally have two categories. One is the garnet ceramic electrolytes (GCEs), which are fabricated by calcinating the garnet powders at a high temperature. The other is the polymer/garnet hybrid electrolytes (PGEs), where garnet powders are well distributed into various polymer matrices to fabricate flexible membranes [10–12]. Each of them shows characteristic advantages and drawbacks. GCEs generally stand out for the excellent ionic conductivities ($>10^{-3}$ S cm^{-1} at 25 °C) and large electrochemical windows (>5 V) [13]. However, their mechanical brittleness and stiffness not only bring interfacial issues with electrode materials but also cause extra difficulties in cell assembly [14,15]. In comparison, PGEs show good flexibility to ensure enhanced interfacial contact with the electrodes. Particularly, PGEs with

* Corresponding author.
** Corresponding author.
E-mail addresses: xxguo@qdu.edu.cn (X. Guo), xsun9@uwo.ca (X. Sun).

https://doi.org/10.1016/j.nanoen.2020.104836
Received 22 February 2020; Received in revised form 20 March 2020; Accepted 8 April 2020
Available online 17 April 2020

hierarchical "garnet-in-polymer" (GIP) and "polymer-in-garnet" (PIG) structures can both achieve low interfacial resistances and Li dendrite suppression [16]. However, most PGEs are limited by insufficient ionic conductivities ($<10^{-4}$ S cm^{-1} at 25 °C) that need an elevated temperature for working batteries [17,18]. Nonetheless, GCEs and PGEs are a good fit for different applications with various functions according to their pros and cons. PGEs are promising in flexible electronics and electric vehicles, while GCEs are suitable for portable electronics [8].

Although mass production of garnet SSEs in the ambient air is feasible, the garnets can react with CO_2 and H_2O in the air, leading to the Li_2CO_3 passivation layer formed on the garnet surface [19,20]. The effects of surface Li_2CO_3 on garnet SSEs have been long overlooked until it was found that the high interfacial resistance of GCEs with Li metal could be attributed to the Li_2CO_3 passivation layer, instead of an intrinsic lithiophobicity of the garnet surface. Asma Sharaf et al. first studied the relationships between interfacial contact and different surface chemistries [21]. The contact angles of Li_2CO_3 and Li was as large as 142° calculated by density functional theory, showing a poor wettability. Conversely, the contact angle between Li_2CO_3-free GCEs and Li is 62°, which can lead to excellent interfacial contact. The surface Li_2CO_3 is considered as one of main reasons behind the Li dendrite growth at the interface [9,22]. Various approaches have been proposed to suppress the Li_2CO_3 formation or remove Li_2CO_3 after air exposure, including component doping [23], polishing in an inert atmosphere [21,22], and rapid acid treatment [24]. The Li_2CO_3-free GCEs show decreased interfacial resistance from 940 to 26 Ω cm^2 and over 700 h cycling under 0.2 mA cm^{-2} at room temperature [24].

Although many studies report the effects of Li_2CO_3 on GCEs from the ionic conductivity to interfacial contact, little work has addressed the effects of Li_2CO_3 on PGEs when garnet particles are introduced into various polymer matrices as fillers, such as poly(propylene carbonate) (PPC) [25], Poly(ethylene oxide) (PEO) [26], and Poly(vinylidene fluoride) (PVDF) [27,28]. In fact, garnet particles are more air-sensitive to form Li_2CO_3 impurity layers due to their much higher specific surface area than the GCEs [29]. As Li_2CO_3 exhibits the ultralow ionic conductivity of $\sim10^{-8}$ S cm^{-1} even at 200 °C [30], the Li_2CO_3 formed at the grain boundary can greatly decrease the overall ionic conductivities of GCEs by orders of magnitude [31]. Therefore, it is highly expected that the ionic conductivity of PGEs can be improved to some extent if the Li_2CO_3 is removed from the surface of garnet particles. In addition, it is generally acknowledged that the Li^+ migration occurs along the polymer/garnet interfaces at the percolation threshold [25,26]. How the poorly conductive Li_2CO_3 affects the Li^+ transport pathway in PGEs is a pending question, especially in the context of varying garnet content. Therefore, it is worthwhile to revisit the electrochemical properties of PGEs, which should consider the effects of Li_2CO_3.

Herein, the effects of Li_2CO_3 on PGEs are systematically investigated based on PEO/$Li_{6.4}La_3Zr_{1.4}Ta_{0.6}O_{12}$ (LLZTO) from "GIP" to "PIG" structure. The Li_2CO_3 formation and removal on the surface of LLZTO are achieved by air exposure for 1 week and subsequent high-temperature treatment at 600 °C. Previously, we proposed the rapid acid treatment to remove the Li_2CO_3 contaminant on the surface of LLZTO ceramic pellets. However, this approach is not suitable for the LLZTO particles due to the large specific surface area of garnet powders. The post-treatment of filtration and drying could lead to the Li_2CO_3 formation again after acid treatment. The interfacial resistance between Li_2CO_3-free LLZTO pellets and PEO is dramatically decreased from 93.1 to 8.9 Ω at 25 °C, indicating an enhanced Li^+ transport ability at PEO/LLZTO interface after Li_2CO_3 removal. The Li_2CO_3-free PGEs from "GIP" to "PIG" show improved properties compared with Li_2CO_3-containing PGEs, in terms of the ionic conductivity, electrochemical window, and Li^+ transference number (t_+). In addition, the PIG electrolytes with high mechanical strength are chosen for further comparison of Li dendrite suppression. The results show that the Li_2CO_3-free PIG electrolytes (PIG@LCO-free) can operate a longer time with a dendrite-free morphology than Li_2CO_3-containing PIG electrolytes (PIG@LCO) at 0.2 mA cm^{-2} (0.2 mAh cm^{-2}). The cathode-supported SSBs with a vertical aligned $LiFePO_4$ (LFP) cathode and PIG@LCO-free electrolyte also exhibit excellent rate and cycle performance.

2. Experimental section

2.1. Materials preparation

PEO (Mw = 1 × 10^6 g mol^{-1}, Sigma) was dried at 60 °C overnight under vacuum prior to the electrolyte fabrication. $Li_{6.4}La_3Zr_{1.4}Ta_{0.6}O_{12}$ (LLZTO) ceramic powders and LLZTO ceramic pellets were prepared by the conventional solid-state reaction as described in our previous paper [32]. Lithium bis(trifluoromethanesulfonyl)imide (LiTFSI) (99.95%, sigma-Aldrich), anhydrous acetonitrile (ACN, Sigma-Aldrich), Polyvinylidene Fluoride (PVDF, Aladdin), super-P conductive additives (SP, Timcal), $LiFePO_4$ (LFP), and deionized water (H_2O) were used as received.

2.2. Fabrication of LLZTO-air and LLZTO-HT

The LLZTO particles and ceramic pellets were exposed to air at room temperature for 1 month, which can react with H_2O and CO_2 to form Li_2CO_3 on the surface. The LLZTO-HT was obtained by high-temperature treatment, which was conducted by placing the samples in an Al_2O_3 boat and heating to 600 °C for 3 h in a muffle furnace. The atmosphere was Ar gas and heating and cooling rate was 10 °C min^{-1}.

2.3. Fabrication of the composite electrolytes containing LLZTO and PEO

LLZTO-air (or LLZTO-HT) particles with concentrations ranging from 20 to 80 wt% were added into ACN (25 mL) and dispersed by sonication to improve the dispersion. After that, PEO and LiTFSI (EO/Li^+ = 10:1 by mol) were added into the solution and stirred continuously for 8 h. Then, the homogenized colloidal solution was cast onto a glass plate with controlled thickness. The ACN solvent was evaporated in a vacuum oven at 60 °C for 12 h. All procedures that are sensitive to moisture or oxygen were carried out in an Ar-filled glovebox (M-Braun, Germany) with H_2O and O_2 levels below 0.1 ppm. In addition, pure PEO(LiTFSI) membranes were also fabricated for comparison using the same procedure without LLZTO particles.

2.4. Characterizations

The X-ray diffraction (XRD) was performed on the Bruker D2 Phaser with Cu K_α radiation (λ = 1.5406 Å) with 2θ range of 10–80° and collected with a step-width of 0.02° at 20 °C to characterize the crystalline structure of ingredients and synthesized membranes. The scanning electron microscope (SEM, S4800) was employed to determine the morphologies of the surface and cross-section of all samples. The cross-sectional samples were obtained by liquid nitrogen quenching. All the samples for SEM were coated with a thin layer of gold via sputtering. Thermogravimetric Analysis was carried out from room temperature to 600 °C.

2.5. Electrochemical measurements and cell assembly

The ionic conductivity of the SPEs was measured by the NOVOCONTROL spectrometer. The measurements were carried out in the frequency range from 0.01 Hz to 7 MHz. The stainless steel (SS) electrodes sandwiched the SPE to construct block/SPE/block cells. The ionic conductivity σ was calculated based on the following equation:

$$\sigma = t/RA \quad (1)$$

where t represents the thickness of the electrolyte membrane, R is the bulk resistance of electrolytes, and A refers to the contact area between

electrolytes and electrodes.

The Li^+ transference number (t_+) was tested in a Li/SPE/Li cell (Autolab PGSTAT 302 N system). The symmetric battery was polarized with a DC voltage of 10 mV. The AC impedance spectroscopy measurements before and after the polarization process were obtained. t_+ was calculated according to the following equation:

$$t_+ = \frac{I_{(t=\infty)}(\Delta V - I_{(t=0)}R_{(t=0)})}{I_{(t=0)}(\Delta V - I_{(t=\infty)}R_{(t=\infty)})} \quad (2)$$

where ΔV is the applied DC polarization voltage (10 mV), $I_{(t=0)}$ and $R_{(t=0)}$ are the initial current and resistance value, respectively. $I_{(t=\infty)}$ and $R_{(t=\infty)}$ are the steady state current and resistance value after polarization for 3600 s, respectively.

The electrochemical window was examined by linear sweep voltammetry (LSV) of SS/electrolyte/Li cells at 25 °C, which was conducted from 2 to 6V at a scan rate of 10 mVs^{-1} by Arbin BT-2000.

The vertically aligned LFP electrodes were fabricated by blade casting. Typically, the LFP powder, SP and PEO/LITFSI (EO/Li = 10/1) was dissolved in the mixture of ACN and H_2O (v/v = 1/9) with a weight ratio of 8:1:1 to form a slurry and then coated onto Al foil. After that, the Al foil coated with slurry was freeze-dried at −50 °C overnight. The Li metal foil with a thickness of approximately 50 μm was used as the anodes. The 2032-type coin cells were assembled in a LFP/SCE/Li configuration. The cells were galvanostatically charged and discharged between 2.8–3.8 V vs. Li/Li^+ under various current densities.

3. Results and discussion

Firstly, the effects of Li_2CO_3 on Li^+ migration at the PEO/LLZTO interface were investigated based on GCEs and PEO(LiTFSI) layers. LLZTO pellets were fabricated by hot-pressing sintering, which exhibited high ionic conductivity (1.1×10^{-3} S cm^{-1} at 25 °C) and high density (>99%) (Fig. S1) [33]. As shown in Fig. 1a, the as-obtained garnet pellets were aged in air for 1 week. The aged LLZTO pellets are abbreviated as LLZTO-air. During the air exposure, the LLZTO can react with H_2O in air, forming LiOH due to Li^+/H^+ proton exchange (equation (3)) [21,34,35].

$$Li_{6.4}La_3Zr_{1.4}Ta_{0.6}O_{12}\ (s) + x\ H_2O\ (g) \rightarrow Li_{6.4-x}H_xLa_3Zr_{1.4}Ta_{0.6}O_{12}\ (s) + x\ LiOH\ (s) \quad (3)$$

Subsequently, LiOH reacts with CO_2 to form the Li_2CO_3 contaminant on the surface of LLZTO pellets (equation (4)) [36].

$$LiOH\ (s) + 1/2\ CO_2\ (g) \rightarrow 1/2\ Li_2CO_3\ (s) + 1/2\ H_2O\ (g) \quad (4)$$

X-ray diffraction (XRD) was applied to investigate the Li_2CO_3 removal by high-temperature treatment at 600 °C. These treated garnet pellets are abbreviated as LLZTO-HT. As shown in Fig. 1b, the small Li_2CO_3 peak located at 23° disappears after high-temperature treatment [19]. All other diffraction peaks are consistent with the standard pattern of cubic garnet LLZO (PDF#45–0109), indicating excellent thermal stability of LLZTO at 600 °C.

Raman spectroscopy was applied to further identify the Li-containing phases considering a low X-ray scattering factor for Li. Fig. 1c compares the Raman spectra of LLZTO-HT with LLZTO-air pellets. The characteristic peaks at 243, 375, 645, and 728 cm^{-1} can be ascribed to the cubic LLZTO phase, and the first two peaks correspond to the Li–O bonding in the LLZTO structure [24]. The peaks in the LLZTO-air and LLZTO match well with the typical peaks of the cubic LLZTO, indicating no impurity phase formation after high-temperature treatment. The vibration of CO_3^{2-} are observed in LLZTO-air at the intense peaks of 158 and 1090 cm^{-1}, while the peaks of Li_2CO_3 are no longer present after high-temperature treatment [36].

To study the Li^+ interfacial kinetics related to the Li_2CO_3 impurity layer, a trilaminar cell configuration was designed, where a 1 μm-thick PEO(LiTFSI) layer was coated on LLZTO pellets and an Au layer was subsequently sputtered as a current collector (Fig. 1d) [37]. Electrochemical impedance spectroscopy (EIS) was utilized to compare the interfacial resistances ($R_{interface}$) influenced by the Li_2CO_3. The

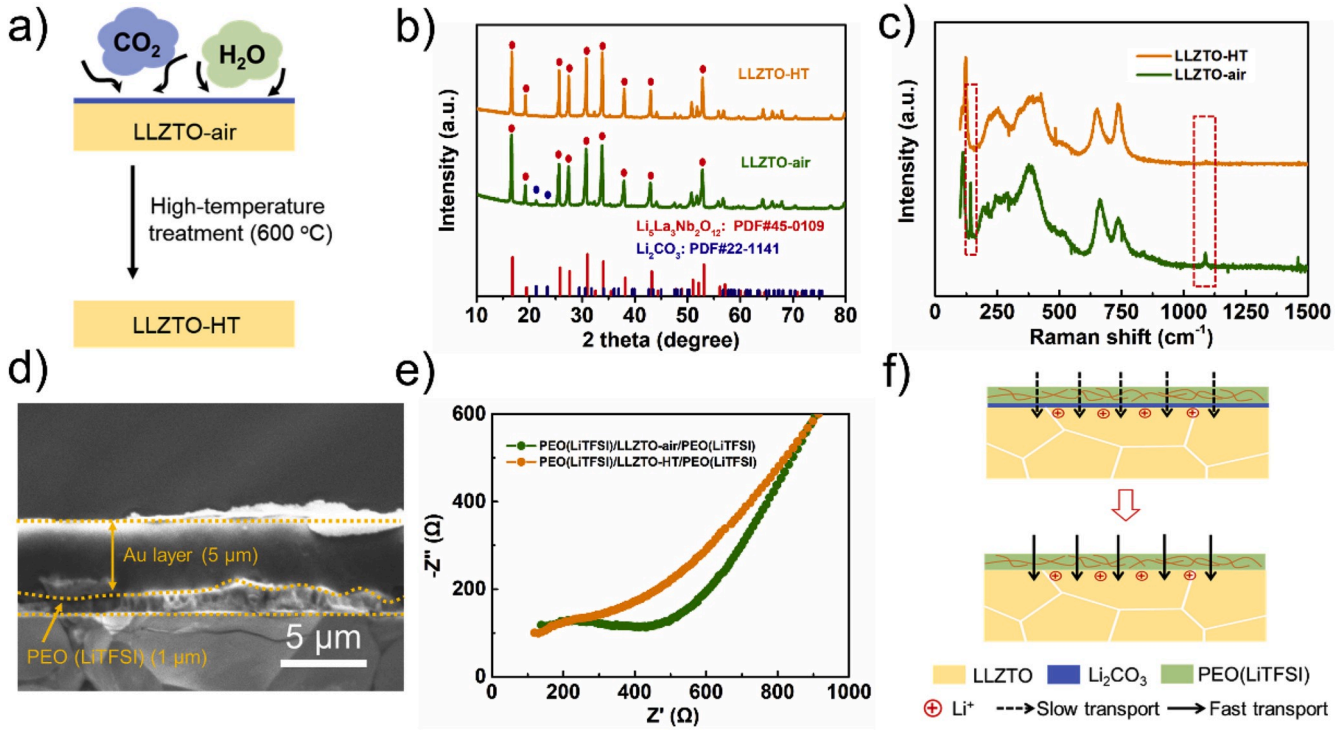

Fig. 1. a) Schematic illustration of Li_2CO_3 formation in air and removal at high-temperature treatment. b) XRD patterns, and c) Raman spectra of LLZTO-air and LLZTO-HT pellets. d) SEM image of interfacial construction for Li^+ transport study at the interface. e) EIS spectra, and f) schematic illustration of enhanced Li^+ transport at the interface by removing the Li_2CO_3 layer.

equivalent circuit is shown in Fig. S9a. The total impedance consists of the resistances from the LLZTO bulk, PEO(LiTFSI) bulk, and the interfaces. As the impedance plots shown in Fig. 1e, the initial point of the spectra corresponds to the resistance of LLZTO bulk. The resistance of PEO(LiTFSI) bulk is calculated according to the ionic conductivity of 3.4 $\times$ 10^{-6} S cm^{-1} for PEO(LiTFSI) (Fig. S2). The $R_{interface}$ between PEO (LiTFSI) and LLZTO-air is 91.3 Ω, while the $R_{interface}$ between PEO (LiTFSI) and LLZTO-HT is 8.9 Ω. The dramatically decreased $R_{interface}$ indicates a faster Li^+ migration across the interface due to the removal of Li_2CO_3 by high-temperature treatment (Fig. 1f).

The LLZTO particles for PGEs were fabricated by solid-state sintering. The diameter of LLZTO particles is approximately 5 μm and the thickness of the Li_2CO_3 layer is ~40 nm after air exposure of 1 week (Figs. 2a and S3). The content of surface Li_2CO_3 is ~2.7 wt% according to the TGA curve (Fig. S4). As XRD patterns shown in Fig. S5, the intensity of the Li_2CO_3 peak at approximately 23° in LLZTO-air particles is greatly decreased after the high-temperature treatment at 600 °C. It should be noted that the high-temperature treatment at 600 °C maybe not totally remove the Li_2CO_3 on the surface of LLZTO particles. The decomposition of Li_2CO_3 is over 750 °C, which was reported in previous studies [38]. We also tried to totally decompose the Li_2CO_3 contaminant at a higher temperature of 750 °C. However, the XRD pattern in Fig. S6 shows that the impurity phase of $La_2Zr_2O_7$ is generated due to the Li loss at 750 °C. In addition, the peaks of the cubic garnet phase are split due to the transition from the cubic phase to the tetragonal phase. Therefore, a relatively low temperature is more proper considering an intact cubic LLZO phase after high-temperature treatment. Raman mappings in a 30 $\times$ 30 μm^2 area were carried out on LLZTO-air and LLZTO-HT samples (Fig. 2b). The color corresponds to the intensity integral of the CO_3^{2-} characteristic peak located at 1090 cm^{-1}. The LLZTO-air exhibits strong Raman signals of CO_3^{2-}, while the Li_2CO_3-free morphology is obtained on the surface of LLZTO-HT, which is consistent with the XRD results.

Compared with the Li^+ migration through the interface between a GCE and a thin PEO layer, the Li^+ migration in PGEs is much more complicated due to the interactions between LLZTO particles and the PEO polymer matrix, such as decreased PEO crystallinity through the addition of LLZTO fillers and the Lewis acid-base effect between the Li salt and LLZTO [39]. To investigate the effects of Li_2CO_3 on the PGEs, PEO/LLZTO electrolytes with various contents (20, 50, and 80 wt%) of LLZTO-air and LLZTO-HT particles were fabricated by blade casting method, respectively. As shown in Fig. 2c–f, the PGEs with 20 wt% garnet particles (either LLZTO-air or LLZTO-HT) show typical "GIP" characteristics, where a small fraction of LLZTO powders are uniformly distributed in the PEO matrix. These two "GIP" electrolytes are denoted as GIP@LCO and GIP@LCO-free, respectively. When the concentration of LLZTO is increased to 80 wt%, the PEO polymer is observed to fill the gaps between garnet particles because of the LLZTO particles as the majority in the electrolyte (Fig. 2e–h). These two "PIG" electrolytes are abbreviated as PIG@LCO and PIG@LCO-free, respectively. The composite electrolytes with 50 wt% garnet powders are in the transition between "GIP" and "PIG", rendering an intermediate state (Fig. 2d–g). The thicknesses of all PEO/LLZTO electrolytes are approximately 100 μm.

Ionic conductivities were tested by EIS at 25 °C (Fig. S2). The equivalent circuit is shown in Fig. S9b. As shown in Fig. 3a, the Li_2CO_3-free electrolytes show higher ionic conductivities than Li_2CO_3-containing electrolytes. However, the underlying mechanisms may be quite different due to the differing Li^+ migration pathways between GIP and PIG (Fig. 3d). Considering GIPs, 20 wt% garnet particles can weaken the crystallinity of the polymer matrix, leading to an enhanced ionic conductivity by improving the segmental motion of the PEO chains [25]. Most importantly, a continuous interfacial channel is constructed to transport Li^+ along the interface between LLZTO particles and the PEO chains beneficial from the percolation effect [40,41]. Li_2CO_3 exhibits an extremely poor ionic conductivity, which hinders rapid Li^+ migration along the interface. Therefore, GIP@LCO-free shows a higher ionic conductivity of 5.5 $\times$ 10^{-5} S cm^{-1} than that of GIP@LCO (3.4 $\times$ 10^{-5} S cm^{-1}) due to the removal of Li_2CO_3 at the interface. When the content of

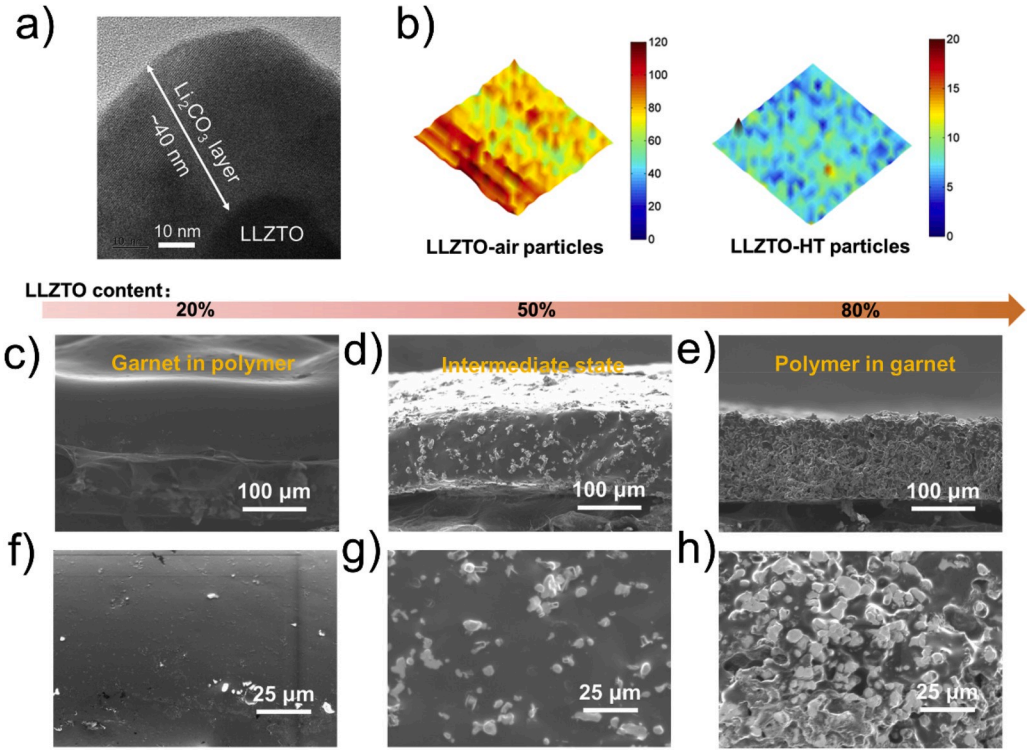

Fig. 2. a) TEM image of LLZTO-air particles. b) Raman mapping images of LLZTO-air and LLZTO-HT particles at 1090 cm^{-1}. Cross-sectional SEM images of composite electrolytes with a c) garnet-in-polymer state, d) intermediate state, and e) polymer-in-garnet state. f-h) Top-view SEM images of composite electrolytes with big magnifications.

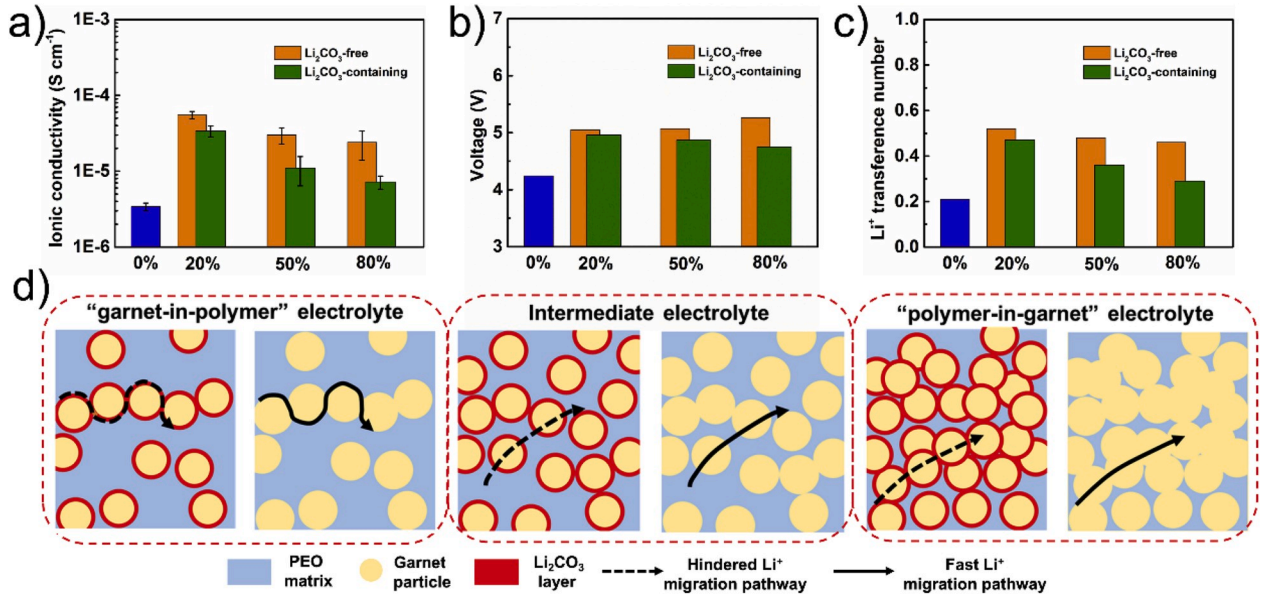

Fig. 3. a) Ionic conductivities, b) electrochemical windows, and c) Li^+ transference numbers of Li_2CO_3-free and Li_2CO_3-containing composite electrolytes with different content of LLZTO particles. d) Schematic illustrations of the Li_2CO_3 effects on Li^+ transport pathways in the composite electrolytes.

LLZTO surpasses the percolation threshold, the interfacial Li^+ transport pathway is hindered, thus leading to a decreased ionic conductivity. At this moment, Li_2CO_3 impedes Li^+ transportation between the PEO matrix and the LLZTO bulk. Further increasing the amount of LLZTO to PIG, the accumulated LLZTO particles can block the movement of polymer chains and decrease the Li^+ conductivity in the PEO region. Li^+ tends to transport via the LLZTO bulk in PIGs, which can also be hindered by the Li_2CO_3 passivation layer [10]. PIG@LCO-free renders an enhanced Li^+ migration through the continuous LLZTO particles, which increases the ionic conductivity from 7.2×10^{-6} S cm^{-1} to 2.4×10^{-5} S cm^{-1}. Note that PIG@LCO-free shows much more obvious ionic conductivity improvement than its GIP counterpart.

As shown in Fig. 3b and S7, the electrochemical windows of the Li_2CO_3-free composite electrolytes are larger than those of Li_2CO_3-containing electrolytes with the same LLZTO contents. The extended electrochemical windows could be attributed to two reasons. On one hand, the Li_2CO_3 starts to decompose as low as 3.2 V [24]. The higher Li_2CO_3 content induces a lower electrochemical window. The electrochemical window of Li_2CO_3-containing electrolytes decreases from 4.96 to 4.75 V with the LLZTO-air content increasing from 20 to 80%, while the Li_2CO_3-free electrolyte can remain at an oxidation voltage over 5 V. On the other hand, the introduction of LLZTO particles into the PEO matrix can enhance the electrochemical stability due to the adsorption of impurities at the PEO/LLZTO interfaces, such as moisture. Compared with the low electrochemical window of pure PEO(LiTFSI) at 4.24 V, the composite electrolytes show increased oxidation voltage both with and without Li_2CO_3 coated on the LLZTO surface. However, this is much more effective if the interference of Li_2CO_3 passivation layer can be avoided. For example, the oxidation process of PIG@LCO commences at 4.75 V, while the sweep of PIG@LCO-free can be extended to 5.26 V without an obvious current.

A high Li^+ transference number (t_+) is significant for SSEs to allow smooth Li^+ migration and suppress the Li dendrite growth [39]. However, polymer-based electrolytes usually show a low t_+ due to the decomposition of the Li salt. The free-mobile anions from the salt hinder the Li^+ uniform transport, forming a space charge near the Li anodes. Therefore, Li dendrites nucleate and propagate through the electrolyte. As shown in Fig. 3c, the t_+ of pure PEO(LiTFSI) is 0.21. Adding LLZTO particles can enhance the t_+ of composite electrolytes due to the Lewis acid-base interactions between LLZTO and PEO polymer [42]. Li_2CO_3-free electrolytes show the t_+ of approximately 0.5 from GIP to PIC, higher than their Li_2CO_3-containing counterparts (Table S1). For example, the t_+ of PIG@LCO-free is 0.49, while that of PIG@LCO is 0.29. This could be attributed to the fact that Li_2CO_3-free LLZTO-HT shows a purer LLZTO surface with acidic groups, which can better share electron pairs with the anions of the Lewis base in PEO polymer. When the anions are immobilized, the t_+ can be improved.

Considering that the high mechanical strength of PIG electrolytes is beneficial for dendrite suppression, Li symmetric cells with PIG@LCO and PIG@LCO-free were assembled to investigate the effect of the removal of Li_2CO_3 on the dendrite suppression capabilities. Cycling was performed at 60 °C to ensure an excellent interfacial contact. The ionic conductivity of PIG@LCO-free at 60 °C is 1.1×10^{-4} S cm^{-1}, while the ionic conductivity of PIG@LCO-containing is 9.2×10^{-5} S cm^{-1} (Fig. S8). Fig. 4a shows that the Li/PEO(LiTFSI)/Li cell short circuits after 150 h cycling at 0.2 mA cm^{-2} (0.1 mAh cm^{-2}). Due to the significant increase in mechanical strength shown by the PIG electrolytes, both Li_2CO_3 free and containing electrolytes exhibit much longer cycle life under the same testing conditions. Both Li/PIG@LCO/Li and Li/PIG@LCO-free/Li can continuously operate over 600 h at 0.2 mA cm^{-2} (Fig. 4a). When the capacity is increased from 0.1 to 0.2 mAh cm^{-2}, the cell with PEO(LiTFSI) shows a shortened cycle life of 19 h due to the poor mechanical strength. Although PIG@LCO shows a high mechanical strength, the Li/PIG@LCO/Li cell renders a gradually increased overpotential from 0.23 to 0.41 V after 200 h cycling and eventually short circuits after 250 h cycling. This could be attributed to the low t_+ of 0.29, which leads to the uneven Li deposition. The high overpotential can act as the driving force to cause Li dendrite growth and eventual short circuit. The SEM images show the mossy-like dendrite morphologies on the surface of Li metal anodes, which is collected from the short-circuit cells (Fig. 4c–d). Conversely, Li/PIG@LCO-free/Li cells can successfully cycle over 600 h with a constant overpotential, indicating stable Li^+ plating/stripping behaviors. This could be attributed to the high t_+ caused by a Li_2CO_3-free structure. SEM images also confirm a dendrite-free morphology on the surface of Li metal from the Li/PIG@LCO-free/Li cell.

To further evaluate the feasibility of Li_2CO_3-free electrolytes for practical applications, different PIG electrolytes with LFP cathodes and Li anodes were assembled into full cells. Considering the cathode-electrolyte interfacial contact is one important issue in SSBs, vertically

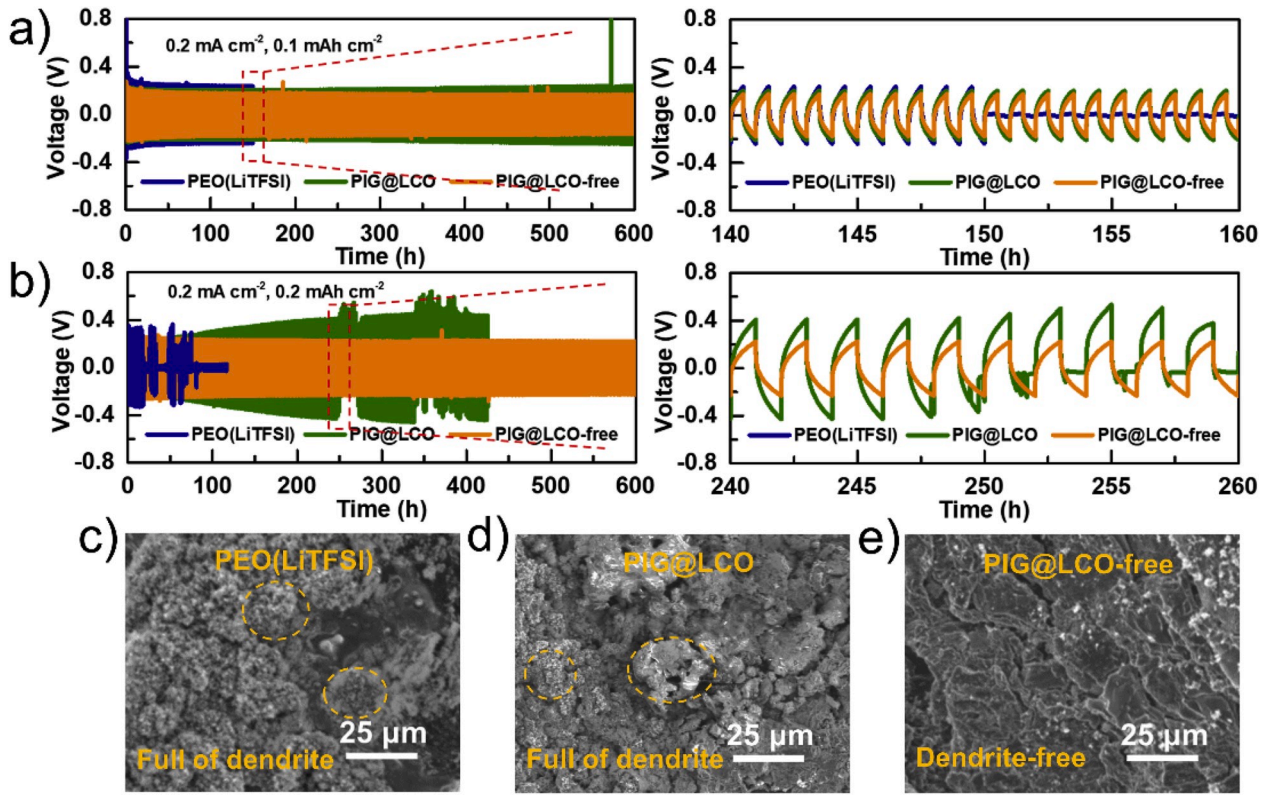

Fig. 4. Voltage profiles of Li symmetrical cells with composite electrolytes at a) 0.2 mA cm^{-2} (0.1 mAh cm^{-2}) and b) 0.2 mA cm^{-2} (0.1 mAh cm^{-2}). SEM images of Li metal anodes after short circuit with c) PEO(LiTFSI), and d) PIC@LCO electrolyte at 0.2 mA cm^{-2} (0.1 mAh cm^{-2}). e) SEM image of Li metal anodes with PIC@LCO-free electrolyte after 600 h cycling at 0.2 mA cm^{-2} (0.1 mAh cm^{-2}). The temperature here for cycling is 60 °C.

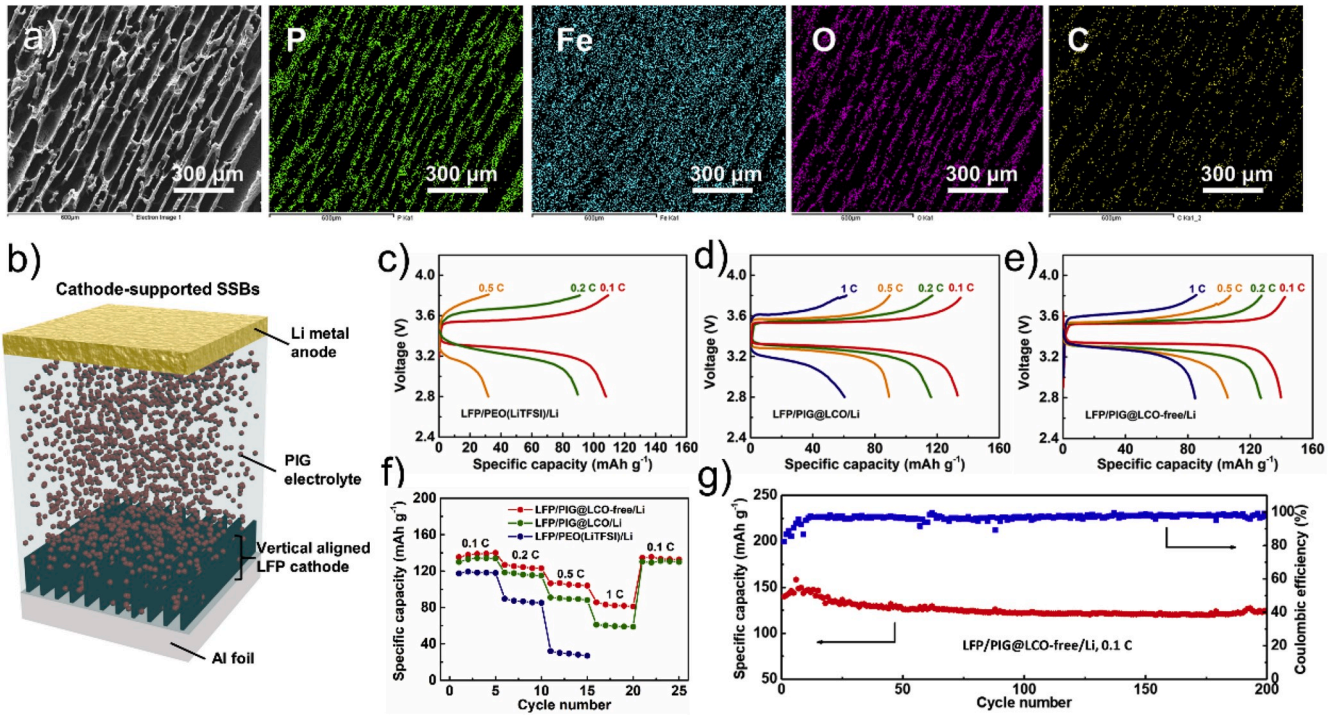

Fig. 5. a) SEM image and EDS mappings of vertical aligned LFP cathode. b) schematic illustration of cathode-supported SSBs. Charge/discharge curves of c) LFP/PEO (LiTFSI)/Li, d) LFP/PIC@LCO/Li, and e) LFP/PIC@LCO-free/Li cells at various rates. f) Rate performance of LFP/Li cells with different composite electrolytes. g) Cycling performance of LFP/PIC@LCO-free/Li cell at 0.1 C.

aligned LFP cathodes were constructed to ensure sufficient bulk Li^+ migration in the cathode (Fig. 5b). The water in composite LFP cathode freezes at −10 °C and the ice is preferentially grown along a vertical direction, leading to the lamellar ice morphology. Under this circumstance, the LFP materials can be pressed into the lamellar structure, leading to the vertical structure after removing ice by freeze-drying. Fig. 5a shows the morphology and relative elemental mappings. The loading of active LFP material is ~6 mg cm^{-2}. It can be divided into "thin LFP electrodes" with a thickness of approximately 20 μm, which effectively reduces the Li^+ transport distance and enhances the Li^+ migration inside LFP cathode. Besides, the electrolyte slurry is poured on the vertical-aligned LFP cathode and well infiltrates the gaps between each lamellar LPF thin cathode. The "cathode-supported" SSBs can decrease the interfacial resistance between LFP cathode and SSEs.

As shown in Fig. 5c, the LFP/PEO(LiTFSI)/Li cell exhibits severe overpotentials and significantly decreased specific capacities upon increasing current rates. It delivers specific discharge capacities of 117.9 and 88.6 mAh g^{-1} at 0.1 and 0.2 C, respectively (Fig. 5f). However, the specific discharge capacity is dramatically decreased to 28.1 mAh g^{-1} at 0.5 C. The low specific capacity and poor cycling performance can be ascribed to the poor Li^+ transport and inhomogeneous Li deposition. Both LFP/PIG@LCO/Li and LFP/PIG@LCO-free/Li cells show smaller polarization and flatter voltage plateaus compared with LFP/PEO (LiTFSI)/Li (Fig. 5d and e). The cells with PIG@LCO and PIG@LCO-free show similar capacities at low rates of 0.1 and 0.2 C. When increasing the rates to 0.5 and 1 C, the capacities of cells with PIG@LCO are 90.2 and 59.4 mAh g^{-1}, while those of cells with PIG@LCO-free are 106.4 and 84.8 mAh g^{-1}. In addition, when returning to 0.1 C after high-rate cycling, the specific capacity of PIG@LCO-free cells can recover to a similar level as before high-rate cycling. The higher capacities of PIG@LCO-free cells could be attributed to the faster Li^+ transport and higher t_+ due to the LLZTO surface Li_2CO_3. With the dendrite-suppressed PIG@LCO-free, an LFP/Li SSB can retain 86.1% of its initial capacity after 200 cycles at 0.1 C at 60 °C (Fig. 5g). Our designed Li_2CO_3-free electrolyte demonstrates great promise for achieving long-lasting dendrite-free SSBs.

4. Conclusion

In summary, the effects of Li_2CO_3 on the PGEs are studied by introducing air-exposed LLZTO and high-temperature treated LLZTO into the PEO matrix. PGEs with various LLZTO contents are fabricated from GIP to PIG. The fundamental electrochemical properties are compared, including ionic conductivity, electrochemical window, and t_+. The GIP@LCO-free shows an improved ionic conductivity of 5.5×10^{-5} S cm^{-1} at 25 °C due to the enhanced Li^+ transport at the interface, while the PIG@LCO-free exhibits an increased ionic conductivity of 2.4×10^{-5} S cm^{-1} due to the Li^+ smooth migration through the LLZTO bulk. A large electrochemical window over 5 V and high t_+ of 0.5 are achieved in the Li_2CO_3-free PGEs from GIP to PIG. The Li/PIG@LCO-free/Li cells can continuously operate over 600 h at 0.2 mA cm^{-2} (0.2 mAh cm^{-2}) with a dendrite-free morphology. In addition, cathode-supported SSBs with a vertical aligned LFP are constructed to address the cathode interfacial issue and enhance the Li^+ transport in the cathode. Such cathode-suppressed SSBs with the PIG@LCO-free electrolytes retain 86.1% of their initial capacity after 200 cycles at 0.1 C. This work is the first to focus on the special surface chemistry of garnet particles and will guide the improved design of PGEs for dendrite-free Li metal SSBs with high safety and high energy density.

Declaration of competing interest

The authors declare that they have no known competing financial interests or personal relationships that could have appeared to influence the work reported in this paper.

CRediT authorship contribution statement

Hanyu Huo: Writing - original draft, Writing - review & editing. **Xiaona Li:** Writing - review & editing. **Yipeng Sun:** Writing - review & editing. **Kieran Doyle-Davis:** Writing - review & editing. **Jianwen Liang:** Writing - review & editing. **Xuejie Gao:** Writing - review & editing. **Ruying Li:** Data curation. **Huan Huang:** Funding acquisition. **Xiangxin Guo:** Supervision, Project administration, Writing - review & editing. **Xueliang Sun:** Supervision, Project administration, Writing - review & editing.

Acknowledgements

H. H. conceived and designed the experimental work and prepared the manuscript; Dr. X. Li. and Y. S. and R. L. helped with SEM characterizations; X. L. did the Raman characterizations; K. D. D. edited and helped with the manuscript. Dr. J. L. did the XRD tests; X. G. help with the vertical aligned LFP cathodes; X. G. and X. S. supervised the overall project. All authors reviewed the manuscript. The authors would like to thank the National Key R&D Program of China (Grant No.2018YFB0104300), the National Natural Science Foundation of China (Grant No. 51771222, 51532002), the "Taishan Scholars Program", Natural Sciences and Engineering Research Council of Canada (NSERC), Canada Research Chair Program (CRC), Glabat Solid-State Battery Inc., and University of Western Ontario.

Appendix A. Supplementary data

Supplementary data to this article can be found online at https://doi.org/10.1016/j.nanoen.2020.104836.

References

[1] Y.-S. Hu, Y. Lu, ACS Energy Lett 4 (2019) 2689–2690.
[2] J.-M. Tarascon, M. Armand, Nature 414 (2001) 359–367.
[3] M. Armand, J.-M. Tarascon, Nature 451 (2008) 652–657.
[4] C.W. Sun, J. Liu, Y.D. Gong, D.P. Wilkinson, J.J. Zhang, Nano Energy 33 (2017) 363–386.
[5] N.J. Dudney, J.B. Bates, R.A. Zuhr, C.F. Luck, J.D. Robertson, Solid State Ionics 53 (1992) 655–661.
[6] J.H. Kennedy, S. Sahami, S.W. Shea, Z.M. Zhang, Solid State Ionics 18–19 (1986) 368–371.
[7] R. Murugan, V. Thangadurai, W. Weppner, Angew. Chem. Int. Ed. 46 (2007) 7778–7781.
[8] N. Zhao, W. Khokhar, Z. Bi, C. Shi, X. Guo, L.-Z. Fan, C.-W. Nan, Joule 3 (2019) 1190–1199.
[9] A.J. Samson, K. Hofstetter, S. Bag, V. Thangadurai, Energy Environ. Sci. 12 (2019) 2957–2975.
[10] L. Chen, Y. Li, S.-P. Li, L.-Z. Fan, C.-W. Nan, J.B. Goodenough, Nano Energy 46 (2018) 176–184.
[11] S. Li, S.Q. Zhang, L. Shen, Q. Liu, J.B. Ma, W. Lv, Y.B. He, Q.H. Yang, Adv. Sci. 7 (2020), 1903088.
[12] T. Jiang, P. He, G. Wang, Y. Shen, C.W. Nan, L.Z. Fan, Adv. Energy Mater. (2020), 1903376.
[13] V. Thangadurai, S. Narayanan, D. Pinzaru, Chem. Soc. Rev. 43 (2014) 4714–4727.
[14] H. Huo, Y. Chen, R. Li, N. Zhao, J. Luo, J.G. Pereira da Silva, R. Mücke, P. Kaghazchi, X. Guo, X. Sun, Energy Environ. Sci. 13 (2020) 127–134.
[15] S.-S. Chi, Y. Liu, N. Zhao, X. Guo, C.-W. Nan, L.-Z. Fan, Energy Storage Mater 17 (2019) 309–316.
[16] H. Huo, Y. Chen, J. Luo, X. Yang, X. Guo, X. Sun, Adv. Energy Mater. 9 (2019), 1804004.
[17] Q. Zhou, J. Ma, S. Dong, X. Li, G. Cui, Adv. Mater. 31 (2019), 1902029.
[18] L. Yue, J. Ma, J. Zhang, J. Zhao, S. Dong, Z. Liu, G. Cui, L. Chen, Energy Storage Mater 5 (2016) 139–164.
[19] W. Xia, B. Xu, H. Duan, X. Tang, Y. Guo, H. Kang, H. Li, H. Liu, J. Am. Ceram. Soc. 100 (2017) 2832–2839.
[20] K. Hofstetter, A.J. Samson, S. Narayanan, V. Thangadurai, J. Power Sources 390 (2018) 297–312.
[21] A. Sharafi, E. Kazyak, A.L. Davis, S. Yu, T. Thompson, D.J. Siegel, N.P. Dasgupta, J. Sakamoto, Chem. Mater. 29 (2017) 7961–7968.
[22] H. Zheng, S. Wu, R. Tian, Z. Xu, H. Zhu, H. Duan, H. Liu, Adv. Funct. Mater. (2019), 1906189.
[23] Y. Li, B. Xu, H. Xu, H. Duan, X. Lu, S. Xin, W. Zhou, L. Xue, G. Fu, A. Manthiram, J. B. Goodenough, Angew. Chem., Int. Ed. Engl. 56 (2017) 753–756.
[24] H. Huo, Y. Chen, N. Zhao, X. Lin, J. Luo, X. Yang, Y. Liu, X. Guo, X. Sun, Nano Energy 61 (2019) 119–125.

[25] H. Huo, J. Sun, C. chen, X. Meng, M. He, N. Zhao, X. Guo, J. Power Sources 383 (2018) 150–156.
[26] H. Huo, N. Zhao, J. Sun, F. Du, Y. Li, X. Guo, J. Power Sources 372 (2017) 1–7.
[27] X. Zhang, T. Liu, S. Zhang, X. Huang, B. Xu, Y. Lin, B. Xu, L. Li, C.W. Nan, Y. Shen, J. Am. Chem. Soc. 139 (2017) 13779–13785.
[28] H. Huo, X. Li, Y. Chen, J. Liang, S. Deng, X. Gao, K. Doyle-Davis, R. Li, X. Guo, Y. Shen, C.-W. Nan, X. Sun, Energy Storage Mater (2019), https://doi.org/10.1016/j.ensm.2019.12.022. Elsevier, In press.
[29] H. Huo, J. Luo, V. Thangadurai, X. Guo, C.-W. Nan, X. Sun, ACS Energy Lett 5 (2019) 252–262.
[30] M. Dissanayake, B.-E. Mellander, Solid State Ionics 21 (1986) 279–285.
[31] W. Xia, B. Xu, H. Duan, Y. Guo, H. Kang, H. Li, H. Liu, ACS Appl. Mater. Interfaces 8 (2016) 5335–5342.
[32] Y. Li, Y. Cao, X. Guo, Solid State Ionics 253 (2013) 76–80.
[33] F. Du, N. Zhao, Y. Li, C. Chen, Z. Liu, X. Guo, J. Power Sources 300 (2015) 24–28.
[34] C. Ma, E. Rangasamy, C. Liang, J. Sakamoto, K.L. More, M. Chi, Angew. Chem., Int. Ed. Engl. 54 (2015) 129–133.
[35] L. Cheng, E.J. Crumlin, W. Chen, R. Qiao, H. Hou, S. Franz Lux, V. Zorba, R. Russo, R. Kostecki, Z. Liu, K. Persson, W. Yang, J. Cabana, T. Richardson, G. Chen, M. Doeff, Phys. Chem. Chem. Phys. 16 (2014) 18294–18300.
[36] A. Sharafi, S. Yu, M. Naguib, M. Lee, C. Ma, H.M. Meyer, J. Nanda, M. Chi, D. J. Siegel, J. Sakamoto, J. Mater. Chem. 5 (2017) 13475–13487.
[37] A. Gupta, J. Sakamoto, Electrochem. Soc. Interface. 28 (2019) 63–69.
[38] Y. Li, X. Chen, A. Dolocan, Z. Cui, S. Xin, L. Xue, H. Xu, K. Park, J.B. Goodenough, J. Am. Chem. Soc. 140 (2018) 6448–6455.
[39] H.Y. Huo, B. Wu, T. Zhang, X.S. Zheng, L. Ge, T.W. Xu, X.X. Guo, X.L. Sun, Energy Storage Mater 18 (2019) 59–67.
[40] W. Wang, E. Yi, A.J. Fici, R.M. Laine, J. Kieffer, J. Phys. Chem. C 121 (2017) 2563–2573.
[41] H. Yamada, A.J. Bhattacharyya, J. Maier, Adv. Funct. Mater. 16 (2006) 525–530.
[42] J. Zhang, N. Zhao, M. Zhang, Y. Li, P.K. Chu, X. Guo, Z. Di, X. Wang, H. Li, Nano Energy 28 (2016) 447–454.